Icarus 204 (2009) 399–408

Contents lists available at ScienceDirect

Icarus

journal homepage: www.elsevier.com/locate/icarus

Elliptical structure of the lunar South Pole-Aitken basin

Ian Garrick-Bethell *, Maria T. Zuber

Department of Earth, Atmospheric and Planetary Sciences, Massachusetts Institute of Technology, 54-521, 77 Massachusetts Avenue, Cambridge, MA 02139, United States

ARTICLE INFO

Article history:
Received 5 June 2008
Revised 12 May 2009
Accepted 15 May 2009
Available online 25 June 2009

Keyword:
Moon

ABSTRACT

The South Pole-Aitken basin (SP-A) is the largest and oldest basin on the Moon. The basin has usually been interpreted to exhibit a degraded circular structure, but here we demonstrate that the topography, iron and thorium signatures of the basin are well described by ellipses with axes measuring 2400 by 2050 km and centered at −53°, 191°E. Topography, abundances of iron, thorium, and the distribution of mare basalts are all elevated in the northern halves of the ellipses. We also identify an outer topographic ellipse whose semiminor axis scales with the main topographic ellipse by approximately $\sqrt{2}$. Taken together, these data imply that the basin was created by an oblique impact along an azimuth of approximately 19°, measured counterclockwise from longitude 191°E. The geometry of the elevated central farside topography surrounding SP-A suggests that it predates the impact. The elliptical ring structures of SP-A and their scaling relationships will help to understand the formation of large and elliptical basins elsewhere in the Solar System. This refined basin shape will also inform local geology, geochemistry, and geophysics of the region.

1. Introduction

Located on the lunar southern farside between the crater Aitken and the south pole, the South Pole-Aitken basin (SP-A) is the largest verified basin on the Moon. The structure is large enough to be classified as one of the three major lunar terranes (Jolliff et al., 2000), and its highly-degraded appearance and abundance of superimposed craters suggests that it may predate all other lunar basins (Wilhelms, 1987). The impactor likely excavated lower crustal materials, and possibly even the upper mantle (Pieters et al., 2001). Samples returned from the basin would provide an opportunity to not only date the oldest preserved cataclysmic event on the Moon, but also to understand the mineralogy of the lunar crust. Because of its large size, SP-A is also important in understanding the formation of massive basins in general (Andrews-Hanna et al., 2008; Marinova et al., 2008).

Despite the importance of the basin, its gross shape and structure are not well understood, with most previous analyses assuming circularity (Hiesinger and Head, 2004; Petro and Pieters, 2004; Pieters et al., 2001, 1997; Spudis et al., 2008, 1994; Stuart-Alexander, 1978; Wilhelms, 1987; Wilhelms et al., 1979; Wood and Gifford, 1980; Yingst and Head, 1997). Schultz (1997) suggested an oblique impact based on the basin's relatively shallow depression, but did not address the shape of the depression. Shevchenko et al. (2007) mapped generally oval-like structures in SP-A based on its topography and also proposed an oblique impact. Extending our preliminary work (Garrick-Bethell, 2004), we quantify the shapes of boundaries of the topography, iron and thorium content of the region. We show that even under loose data selection criteria the distributions of these three quantities trace elliptical shapes that are oriented along the same azimuth, have nearby centers, similar eccentricities, and centers that lie along their common azimuth. This high coincidence of fit parameters from the three datasets suggests that ellipses represent a good fit to the data, and demonstrate that SP-A is an elliptical structure that formed from an oblique impact. We also expand the best-fit topographic ellipse outward to identify an additional elliptical-shaped topographic contour, nearly concentric to the original fit, whose semiminor axis follows approximately $\sqrt{2}$-proportional spacing. This ellipse passes near massifs originally used to map the outer extent of the basin (Stuart-Alexander, 1978; Wilhelms, 1987; Wilhelms et al., 1979), and provides a better fit than the circular rings used in these earlier studies. Characterization of the elliptical shape of the South Pole-Aitken basin provides a context for understanding the basin's effect on regional geology, mineralogy, geochemistry, gravity, state of compensation, and the effect of the basin on the Moon's orientation.

2. Data

Topography data are from a spherical harmonic expansion of Clementine laser altimeter data, mapped at 0.25 pixel per degree resolution, referenced to a spheroid of radius 1738 km at the equator, with flattening of 1/3234.93 corresponding to the flattening of

* Corresponding author. Address: Massachusetts Institute of Technology, 54-520, 77 Massachusetts Avenue, Cambridge, MA 02139, United States.
E-mail address: iang@mit.edu (I. Garrick-Bethell).

0019-1035/$ - see front matter © 2009 Elsevier Inc. All rights reserved.
doi:10.1016/j.icarus.2009.05.032

the geoid (Smith et al., 1997; Zuber et al., 1994). These data are truncated polewards of 70° latitude, leading us to also use global topography data from the Unified Lunar Control Network (ULCN2005) (Archinal et al., 2006). We use thorium and iron (FeO) data from the Lunar Prospector gamma-ray spectrometer, mapped at 0.5 pixel per degree resolution (Lawrence et al., 2003, 2002). We chose to use iron and thorium data because these data have the highest resolution and fidelity compared to data for other elements. Iron and thorium are also useful for estimating the depth of excavation of the impact, since iron is indicative of deeper crustal and upper mantle mineralogy, while thorium is a proxy for KREEP-rich material (potassium, rare Earth elements, and phosphorous) that is believed to have crystallized between the lower crust and mantle.

An important test of the significance of our derived ellipses is their correlation with observable geologic features in SP-A. Our ellipses are derived from very large-scale patterns of relatively low-resolution data, and if they are representative of the formation mechanism and structure of SP-A, we would expect a correlation with smaller features that are characteristic of major lunar basins, such as arcuate mountains or ring-like structures. Traditionally, basin rings on the Moon have been identified using high phase-angle photographs (Hartmann and Kuiper, 1962; Head, 1974; Spudis, 1993; Wilhelms, 1987; Wilhelms et al., 1979), where shadows are exaggerated and morphology is readily apparent. Therefore, to test our predictions and compare them with the results of past efforts to map SP-A's rings, we examine two regions in SP-A where high phase-angle images are available. The first is an image from the Apollo 8 Hasselblad camera, taken of the northeastern rim of the basin, and the second is a mosaic of high latitude Clementine 750 nm reflectance images at the south pole (produced by the USGS). The two regions imaged are located on almost opposite sides of the basin.

Two additional useful data sets can be used to further constrain the utility of our ellipses. The first is the global Clementine 750 nm spectral reflectance mosaic, in which the SP-A basin appears as a dark mafic anomaly (Belton et al., 1992). We will test if the anomalously low-albedo region is enclosed by the ellipses. We also apply a spectral band ratio scheme to Clementine UVVIS data to highlight soil maturity and mineralogical differences. The scheme was used by Pieters et al. (1994), and assigns red = 750/415 nm, green = 750/950 nm, and blue = 415/750 nm. This color scheme highlights many of the spectral features present in the lunar surface. In particular, high iron content is indicated by strong absorption near 1-μm (herein the 950 nm band), or stronger green and yellow tones. Soil maturity and composition are reflected by the steepness of the visible continuum slope, which is quantified by the 750 and 415 nm ratios (red to blue variations). The SP-A region has a distinctively orange and green (iron-rich and mafic) character that we can test for a correlation with the topographic ellipses. In addition to testing the validity the ellipses, both of these data sets are also essential for visualizing how the basin's ellipses correlate with other geologic features such as Mare Ingenii, Mare Australe, the Apollo basin, the Schrödinger basin, Jules Verne Crater, and the lunar south pole. We note that all of the Clementine spectral data are subject to high phase-angle artifacts polewards of about 70° latitude (which makes them useful for morphology, above). However, we included high latitude data in our figures so that features polewards of 70° are identifiable, albeit not well represented.

3. Method and results

3.1. Defining distributions of topography, iron, and thorium

When topography, iron, and thorium data are plane-projected from a center of −56° and 180°E (the often-assumed SP-A basin center), it is clear that the quantities are distributed in elliptically-shaped patterns. Unlike a circular crater on a spherical Moon, whose perimeter creates a small circle that can be defined in a plane, the perimeter of an elliptical crater on a sphere is a three-dimensional curve. However, we can fit an ellipse, which is a much simpler shape, to the plane-projected shape to quantify several of the most intrinsic properties of the crater, including its boundaries, center, semimajor axis, a, and semiminor axis, b, and orientation. Because an ellipse is a planar feature that has a formally defined center, the natural choice for projection is an azimuthal projection centered on the ellipse center. Specifically, the stereographic projection is well suited for this task because it is the only commonly used conformal (angle or shape preserving) azimuthal projection,[1] and does not distort small circles centered around the pole of the projection (scale is constant along the circle perimeter). Therefore, the stereographic projection assures that deviations from circularity are readily apparent and easily comparable to purely circular features.

To determine the best-fit ellipse for topography, iron and thorium, we selected data points at the perimeters of their distributions and performed a least-squares fit to the stereographic plane-projected data, while permitting a tilt angle (defined as a rotation within the page about the center of the ellipse). The fitting process was performed for 20 different sets of carefully selected data points and the ellipse parameters from the 20 sets were then averaged to produce the final reported ellipse. The center of the ellipse was determined, and the plane-projected ellipse was then recalculated using the new center, to avoid any minimal distortions due to an off-center projection. The true lunar coordinates of the ellipse edges were then determined and a and b were calculated as great circle arc lengths from the ellipse center to the edges, in both kilometers and degrees (Table 1). We also calculate the ratio a/b to quantify the crater's ellipticity. The final ellipse tilt angle reported is the azimuth of a great circle arc from the ellipse center to the northern end of the semimajor axis, defined relative to a meridian passing through the ellipse center (positive clockwise).

The most obvious uncertainty in this study is how to objectively select the data points that are used to the fit contours. We consider each dataset separately, since there are unique issues associated with each.

To define the primary topographic shape of the basin we used the Clementine laser altimeter data instead of ULCN2005 because ULCN2005 showed some ∼1 km differences with the Clementine laser range values at several locations on the basin perimeter. Also, investigations showed that it made almost no difference which of these data sets is used (below). Later we compare our results with the ULCN2005 data and take advantage of its higher resolution to examine some small-scale geologic features, where relative elevations are of interest and absolute differences in topography are less important. We used 50 data points to establish the topography fit.

In the northern parts of the basin, the elliptical pattern of the topography is most clearly manifested around a −2000 m contour, Fig. 1A. Following the −2000 m contour counterclockwise from the northernmost part of the basin, we find that it is interrupted by a north–south directed feature (A), which we avoided. The contour is interrupted again at Mare Ingenii (B), but continues again at about −37°. We used the contour from (−26°, 197°E) to (−48°, 160°E) in data selection, but did not use any portion within Mare Ingenii, even though examination of the topography data in the ULCN2005 model show that a similar contour continues across Mare Ingenii, albeit at lower elevation. We then followed the

[1] The Lambert conformal conic projection is another option, but would require the choice of two standard parallels. A natural choice may be to make one single standard parallel a pole at the center of the ellipse, but this projection then becomes a stereographic azimuthal projection.

Table 1
Best-fit ellipse parameters assuming a spherical Moon with a radius of 1738 km.

Parameter	Best-fit topography[a]	Outer topography[b]	Iron	Thorium
Center latitude °S	−53.2°	−55.0°	−51.4°	−47.2°
Center longitude °E	191.1°E	191.1°E	188.4°E	185.6°E
Tilt angle (degrees)	−18.8°	−18.8°	−14.1°	−17.0°
Semimajor axis (km)	970	1.238 × 970	1030	940
Semiminor axis (km)	720	1.428 × 720	710	740
Semimajor axis (arc°)	32.0°	39.6°	33.9°	31.0°
Semiminor axis (arc°)	23.7°	33.9°	23.2	24.3°
Semimajor/semiminor axis	1.35	1.17	1.46	1.27
Surface area (% of sphere)	5.7	10.1	5.9	5.6
Northern edge	(−22.3°, 180.4°E)	(−16.6°, 178.7°E)	(−18.1°, 180.2°E)	(−17.2°, 176.5°E)
Southern edge	(−78.4°, 249.1°E)	(−77.7°, 293.3°E)	(−80.4°, 243.5°E)	(−74.4°, 219.7°E)
Eastern edge	(−41.0°, 221.3°E)	(−35.2°, 231.3°E)	(−41.1°, 219.0°E)	(−35.9°, 214.7°E)
Western edge	(−54.2°, 150.6°E)	(−51.6°, 133.0°E)	(−51.1°, 150.9°E)	(−48.6°, 149.0°E)
Great circle azimuth from best-fit topographic center to ellipse center	–	–	−44°	−33°

[a] Parameters derived from Clementine topography. See Section 3.1 for a comparison with ULCN2005 parameters.
[b] Parameters partly derived from best-fit topography; see Section 3.4 for details.

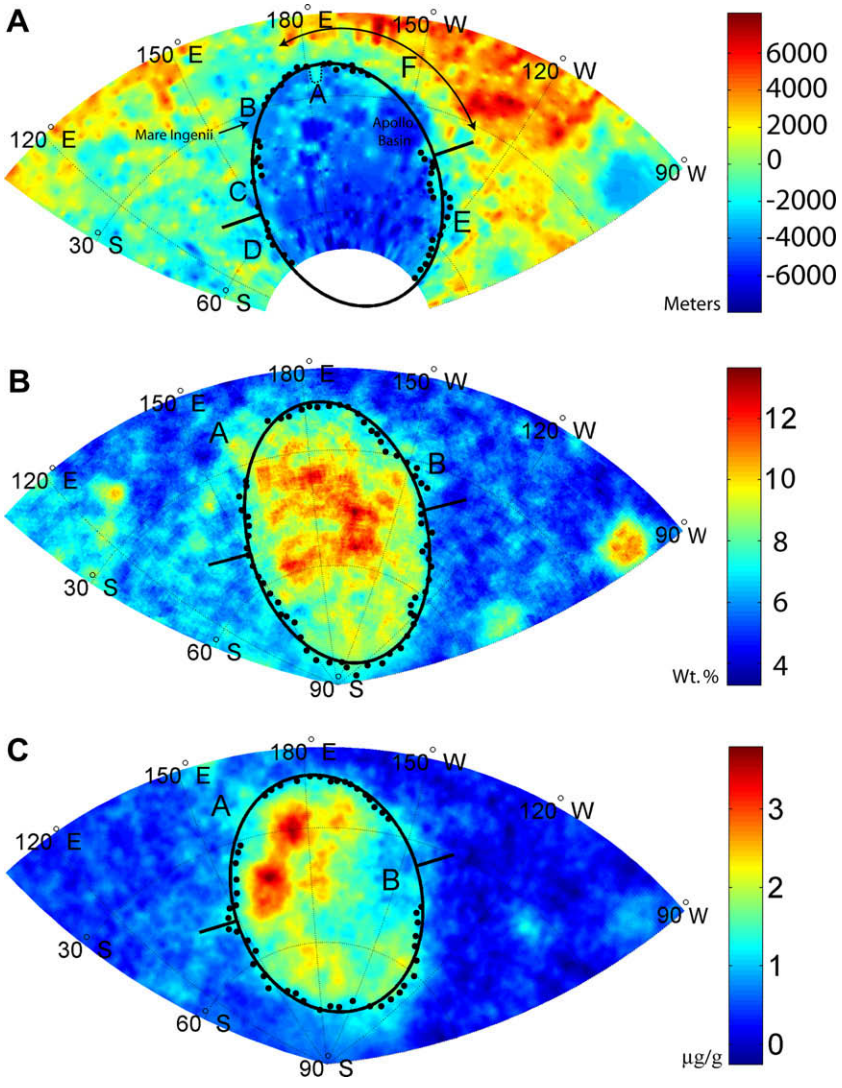

Fig. 1. Best-fit ellipses and representative data used in the fit for: (A) Clementine topography, (B) Lunar Prospector iron (FeO), and (C) Lunar Prospector thorium. Straight lines indicate the ellipse tilt angle. The projection is stereographic and centered on the best-fit center of each ellipse (Table 1). Part A labels: (A) topography not included in fit (dotted line), (B) topography not included in fit due to Mare Ingenii, (C) and (D) topographic depressions not included in fit, (E) topography considered part of the putative ellipse, despite its easterly displaced contour, (F) arcuate topography contour used to derive the outer ellipse. Part B labels: (A) iron data not included in fit due to Mare Ingenii, (B) iron data incorporated into fit, despite the effects of the Apollo Basin. Part C labels: (A) thorium data not included in fit due to Mare Ingenii, (B) thorium data not included in fit due to the effects of the Apollo Basin. See main text for details.

−2000 m contour further southward, not including a depression that extends westward (C) or the crater Planck (D). We eliminated from consideration all data poleward of −70°, and picked up the −2000 m contour again in the east. At approximately (−60°, 240°E), there is an eastern-extending region of low topography (E) that could not be ruled out as part of any putative ellipse. We therefore selected points in this region but excluded data in the vicinity of the Apollo basin. A typical set of data points is shown in Fig. 1A, along with the mean best-fit ellipse and lines about its semiminor axis to illustrate the tilt angle. The best-fit ellipse parameters are listed in Table 1. While this ellipse fits most of the data, it is clear that it does not pass through region E, suggesting region E is not a part of the main ellipse. To indicate the uncertainty in the fit, we note that the standard deviation after averaging the 20 similar elliptical fits was about 1° for the basin center and 2° for the tilt angle. Similar standard deviations were found to be true for the iron and thorium ellipses. Performing the same analysis with ULCN2005 with 65 data points (compared with 50 for Clementine to allow for increased area coverage near the pole) produces a very similar mean ellipse center (−53.2°, 191.8°E), a slightly greater tilt angle of 21.2°, and shorter semi axes, a = 960 km, b = 670 km. The similarity of the values speaks to the robustness of the technique even when limited portions of SP-A's topography contour are used. Second order corrections to our results can always be performed when superior topographic data become available.

The iron data are the most free of features that would complicate the choice of data points around the putative elliptical contour, Fig. 1B. The general approach was to follow the 7.5–8.0 wt.% iron contour with 65 approximately equally-spaced data points. This contour level separates the "inner" and "outer" portions of the SP-A Terrane defined by (Jolliff et al., 2000) and is visibly the most obvious contour. Notably, the northern part of the basin shows the sharpest and most well-defined contour. In the northwest there is a small region of high iron that extends westward (A), which was avoided. On the east side of the basin the iron extends slightly eastward out from the Apollo basin (B), but the contour was still followed. The final mean best-fit iron ellipse is shown in Fig. 1B, as well as a typical set of 65 data points. The ellipse passes close to nearly all points, suggesting that the feature is well described by an elliptical shape.

For thorium, the general approach was to follow the 1.25-ppm contour with 50 approximately equally spaced points. Because the area of the enhanced thorium in SP-A is smaller than the area for iron, fewer data points were used. In the northwest the same region that was elevated in iron is elevated in thorium and was avoided, Fig. 1C (label A). Based on a correlation with basin topography and spectral similarity to other parts of the basin, the high-thorium anomaly in the northwest is likely indigenous to the basin and therefore likely a part of the putative thorium ellipse (Garrick-Bethell and Zuber, 2005; Haskin et al., 2004), but other possibilities include ejecta from the Serenitatis (Wieczorek and Zuber, 2001) or Imbrium basins (Haskin, 1998; Stuart-Alexander, 1978). At any rate, we made no special effort to avoid it. In the east, the Apollo basin seems to have greatly affected the SP-A thorium distribution, as indicated by the c-shaped low-thorium feature (B), possibly because of its internal mare basalt flows. This region was not included in the data selection. Similar to the iron data, the contour is again sharpest and most well defined in the northern part of the basin. The average best-fit ellipse and a typical set of selected data points are shown in Fig. 1C. Again, the data points selected are close to the best-fit ellipse.

We found that using other (non-conformal) azimuthal projections, such as orthographic, gnomonic, Lambert equal area, or Breusing harmonic mean, produced tilt angles that differed by ±0.3°, and semi axes that differed by ±0.1% (in km) compared to the stereographic projection, when using the same plane-projected latitude–longitude points for topography, iron, and thorium. These differences are far lower than the uncertainty from choosing data points.

3.2. Testing the technique

The three best-fit ellipses and their parameters are consistently reproduced using as few as 15 data points, even if selected without care. However, to further test our methodology we fit ellipses (not shown) around the Orientale basin using Lunar Prospector iron (using the edge of the central iron-rich mare) and Clementine topography data (using the Montes Cordillera ring at ∼900 km diameter). We found a basin center of (−19.2°, 265.5°E) from topography and (−19.3°, 265.7°E) from iron, which compare quite favorably with the USGS value of (−19.4°, 267.2°W) for the center of the mare (http://planetarynames.wr.usgs.gov) and (−19°, 265°E) for the basin center (Spudis, 1993).

3.3. Orientations, ellipticities, and great circle azimuths

From Fig. 1 and Table 1 it is clear that the SP-A topography, thorium, and iron distributions are well-fit by ellipses that are oriented towards the west at angles of −18.8°, −17.0°, and −14.1°, respectively. In addition, the azimuth of a great circle drawn from the topographic ellipse center (−53.2°, 191°E) to either the thorium or iron center lies along the same approximate azimuth as the ellipse tilt angles. For example, the azimuth from the topographic center to the center of the thorium ellipse is −33°, measured counterclockwise from longitude 191.1°E (clockwise positive). The azimuth from the topographic center to the center of the iron ellipse is −44°. The center of the iron ellipse is quite close to the center of the topographic ellipse, making the azimuth angle sensitive to changes in iron ellipse center. However, the azimuth to the more northern thorium ellipse center is less sensitive to small changes in location, and is a more reliable number. The thorium and iron ellipse centers are plotted as black squares in Fig. 2C and D in a topographic-ellipse centered coordinate system to illustrate their relationships to the topographic ellipse center.

The ratio a/b for all ellipses are fairly large, 1.27–1.46, with the thorium ellipse the most circular of the three, 1.27, and the iron ellipse the most elliptical, 1.46. Considering the uncertainty in selecting data points, the agreement of the ellipses in tilt angle and axial ratios is quite good, and unlikely to be a coincidence or artifact of our technique. By comparison, the best-fit ellipse for Orientale's topography produces ratios of a/b the range of 1.05–1.07. While we cannot not rule out a modest ellipticity for Orientale, these values are likely large compared to the value defined by the basin's characteristic rings. This is because the complete outline of the basin is difficult to resolve in the Clementine data, as well as the ULCN2005 data, even though the rings are well defined in images. Indeed, using the Cordillera and Outer Rook rings defined in the airbrush map of (Rosiek and Aeschliman, 2001) provides axial ratios of 1.00–1.05. Therefore, SP-A may be considered to significantly deviate from circularity at least compared to Orientale, the often-assumed prototypical multiring basin. However, when compared to at least two other very massive basins, SP-A's axial ratios appears to be typical (1.33 for Hellas and 1.25 for Borealis, both on Mars (Andrews-Hanna et al., 2008)), suggesting that massive basins may in general be more elliptical.

3.4. Multiring structures?

Large basins on the Moon and other bodies often exhibit ring spacing which is commonly proportional to approximately $\sqrt{2}$ (Pike and Spudis, 1987). Does the SP-A basin exhibit multiring

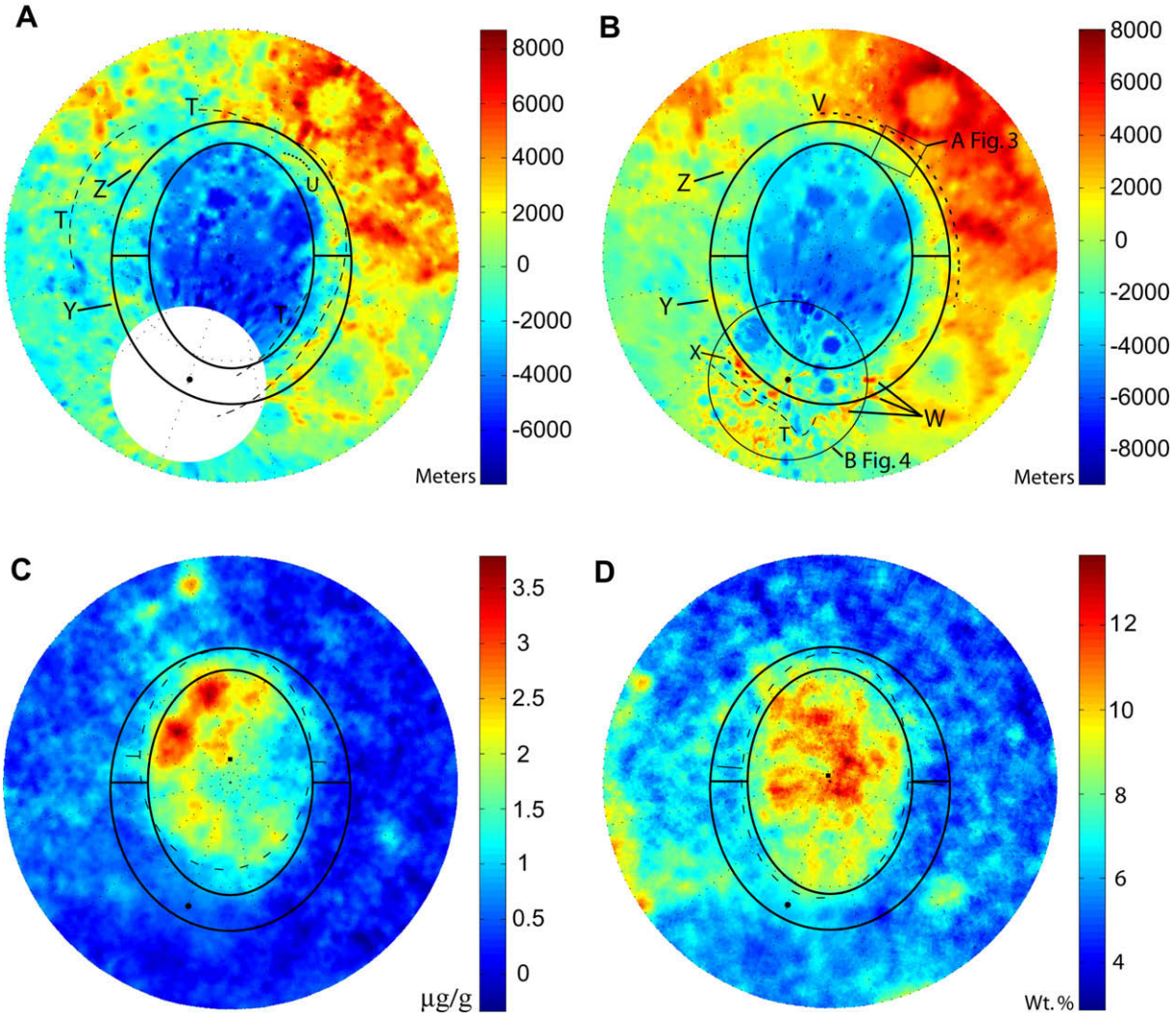

Fig. 2. Best-fit topography ellipse and derived outer ellipse draped over: (A) Clementine topography, (B) ULCN2005 topography, (C) Lunar Prospector thorium with best-fit thorium ellipse (dashed line) and thorium ellipse tilt angle (light solid line), and (D), Lunar Prospector iron (FeO) with best-fit iron ellipse (dashed line) and iron ellipse tilt angle (light solid line). Heavy solid lines in all parts indicate the topography ellipses and their tilt angle (zero in this projection), black dots indicate the south pole, and black squares indicate the thorium and iron ellipse centers in parts (C) and (D). The projections are stereographic centered on the best-fit topographic ellipse center (−53.2°, 191.1°E) and rotated 18.8° clockwise. The limit of the projection is 60° of latitude and gridline spacing is 30°. Part A labels: (T) dashed lines, rings mapped by Wilhelms (1987), (U) dotted line, arcuate massifs in Fig. 3, (Y and Z) high topography possibly related to the outer ellipse. Part B labels: (T) dashed line, rings mapped by Wilhelms (1987), (V) dashed line, arc of high topography associated with the outer ellipse, (W) isolated high topography associated with the outer ellipse, (X) arcuate high topography at the south pole associated with the outer ellipse, (Y) and (Z) isolated high topography possibly related to the outer ellipse.

structures? The best-fit iron and thorium ellipses show no other obvious structure outside of their bounds. However, the topography displays an arcuate structure north and northeast of the basin in the highlands terrain (Fig. 1F). We found an optimal fit to the northern topography using a larger ellipse with a semiminor axis 1.428 times as large as the best-fit topographic semiminor axis, a semimajor axis 1.238 times as large, an ellipse center 2.0° lower in latitude, and the same tilt angle of −18.8°. Interestingly, the scaling in semiminor axis is close to $\sqrt{2}$. The derived outer topographic ellipse is shown plotted over Clementine and ULCN2005 topography data in Fig. 2A and B, respectively (rotated and centered on the best-fit center). The new ellipse not only matches a long arc of topography in the north and northeast (label F in Fig. 1A and label V in Fig. 2B), but also passes through high topography near the south pole in the ULCN2005 map (Fig. 2B, label X), high topography near label W in Fig. 2B, and two other isolated high elevations in the west (labels Y and Z in Fig. 2A and B, more speculative). The axial ratio a/b for this outer ring is 1.17, smaller than for the best-fit topographic ellipse (1.35), and closer to the value for the much larger martian Borealis basin. For convenience we define the area between the best-fit ellipse and the outer ellipse as the Outer Terrace.

We note that Shevchenko et al. (2007) proposed that the deeper topography in the south is a separate ring structure, which cannot be ruled out. However, we found existing topography data to be of inadequate quality to test this hypothesis using our ellipse-fitting method.

3.5. Topography correlation with geologic units

To test whether the topographic ellipses are related to identifiable geologic features and compare our results with the often-used basin outlines of Wilhelms et al. (1979), Wilhelms (1987) and Stuart-Alexander (1978), we examine in more detail regions A and B in Fig. 2B. For region A, we use an oblique south-looking view of northeastern SP-A that shows high mountains on the horizon at approximately −21°, from 198°E to 202°E (∼140 km in extent, originally mapped by Stuart-Alexander (1978) and Wilhelms

(1987) using a similar image). Also shown are several features, transects, and the outermost topographic ellipses mapped onto a Clementine 750 nm reflectance image, overlaid with ULCN2005 topography. Notably, two sections of the outer ellipse coincide with east–west trending hummocks, highlighted by transects 1 and 2. Topography becomes significantly higher when moving north and perpendicular to these hummocks, especially across transect 1. These units are roughly linear and do not perfectly follow the outer ellipse, but each trends generally in the direction of the ellipse and intersects it. The first transect was mapped by Stuart-Alexander (1978) as the northernmost section of SP-A's outer ring.

The prominent mountain range highlighted by transect 3 is between the outer and best-fit topographic ellipses and is nearly concentric with them, but it is not directly associated with either of them. These mountains, which we refer to here as the "Wilsing Mountains" (for the Nectarian age 73-km-diameter crater at (−21.5°, 204.8°E), that encloses the smaller crater labeled L), are also visible in Clementine topography data in Fig. 2A (Label U), and partly in ULCN2005 (Fig. 3). They are almost certainly the result of SP-A basin formation, and the band ratio scheme of (Pieters et al., 1994) shows a distinct change in mineralogy to more iron-rich materials on the south side of the mountains (not shown). Determining whether the Wilsing Mountains are part of a large distinct ring system between the best-fit and outer ellipses, or are local in extent, will require higher-accuracy topography and better high phase-angle images. Overall, however, we find that the correlation of topography with transects 1 and 2 support our choice for the outer ellipse in this region, in agreement with (Stuart-Alexander, 1978).

We next examine terrain in region B of Fig. 2B using a Clementine 750 nm mosaic produced by the USGS, draped with ULCN2005 topography data, Fig. 4. Most importantly, the high topography at label X in Fig. 2B is correlated with arcuate massifs along the dashed line indicated by label P in Fig. 4. These massifs were previously believed to be associated with SP-A based on Earth-based telescopic and Clementine observations (sometimes referred to as the Leibnitz Mountains (Shoemaker et al., 1994)). Massifs that are part of the same arc, but that are not readily apparent in the topography data are labeled at Q. Some of these massifs were also discussed by (Shevchenko et al., 2007) in their efforts to define SP-A's rings, and they are clearly visible in radar backscatter images (Margot et al., 1999). The elevated topography in the region at label S also matches the outer ellipse, but there is no morphologically obvious feature there. The high topography and massifs at R may also be part of the outer ellipse, albeit discontinuous and slightly

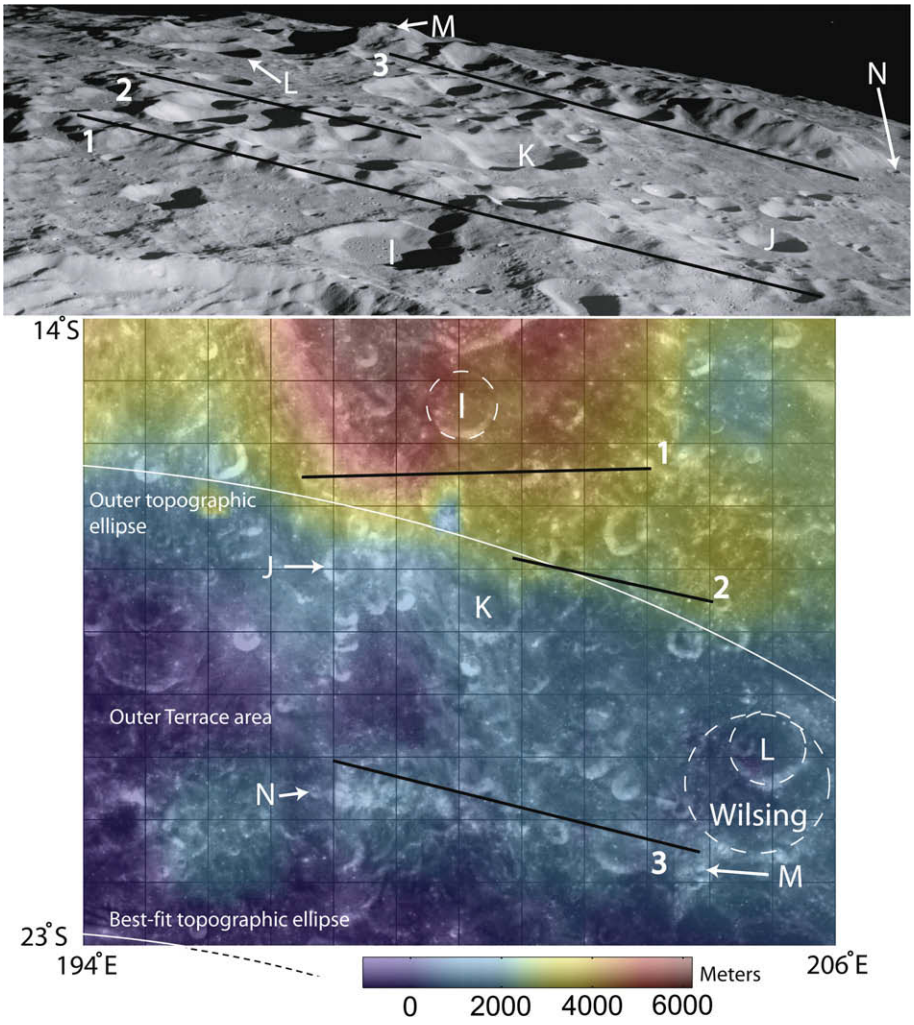

Fig. 3. Top: South-looking oblique view of SP-A basin massifs on the edges of the outer and best-fit topographic ellipses, originally mapped by Stuart-Alexander (1978) and Wilhelms (1987) (Apollo 8 frame H-2319). Bottom: Clementine 750-nm reflectance image with transects from the top panel. Transects: (1) and (2) Massifs correlated with the outer ellipses and mapped as the basin's northern edge by Stuart-Alexander (1978), (3) arcuate massifs not associated with either topographic ellipse. Labels: (I–N) Craters useful for comparing the top and bottom images.

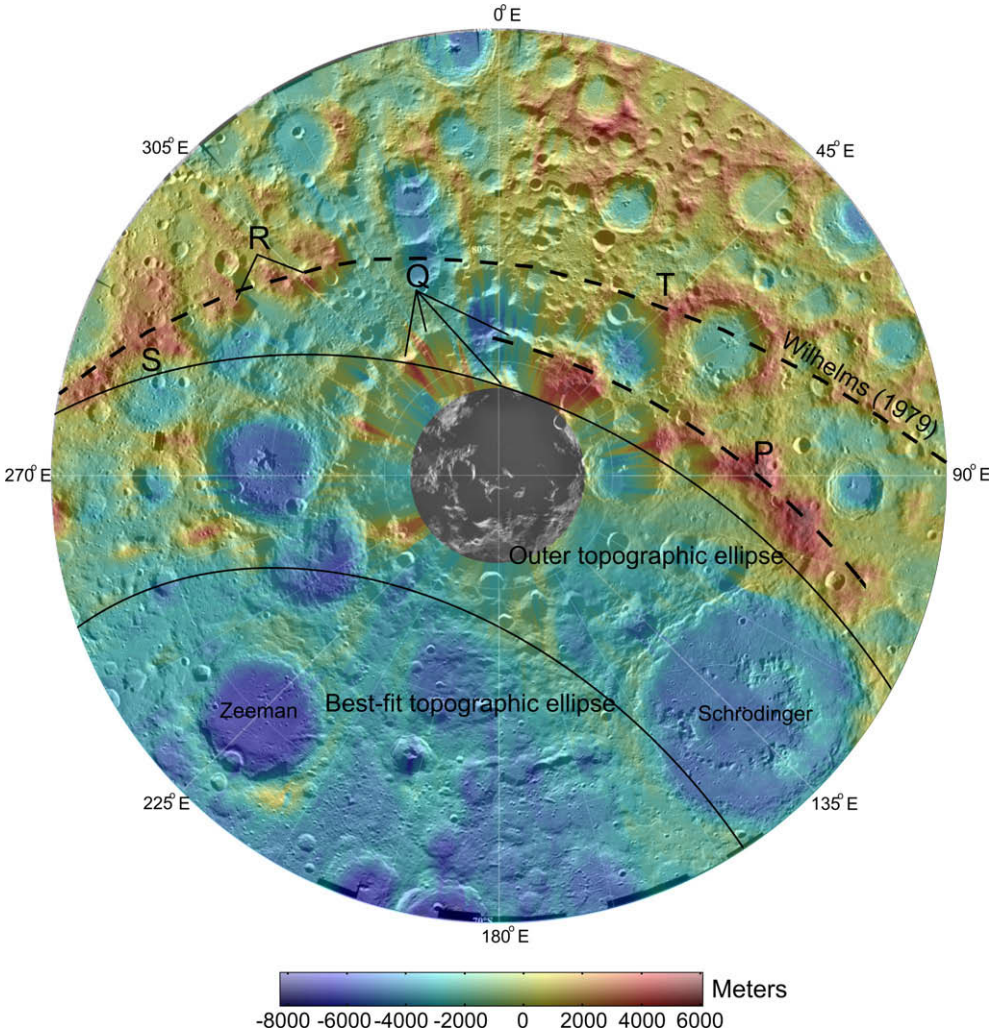

Fig. 4. Orthographic projection of USGS-produced Clementine 750 nm reflectance mosaic draped with UCLN2005 topography, best-fit topographic ellipse, and outer topographic ellipse. The projection is centered at the south pole and extends to 70°S, with 5° parallels shown. Spurious topography data have been masked out near the pole. Labels: (P) Arcuate massifs and high topography associated with the outer ellipse, (Q) massifs not readily apparent in UCLN2005 topography data, (R) massifs, possibly a discontinuous section of the outer ellipse, (S) elevated topography associated with the outer ellipse, (T) outer ring mapped by Wilhelms et al. (1979).

recessed from the main structure. Wilhelms et al. (1979) also mapped an outer SP-A ring near the poles, shown as a dashed line (label T), but this ring misses the more prominent massifs at P, and is not concentric with them. The correlation of our ellipse with terrain using superior photographic and topographic data suggest that our mapping is more appropriate.

Wilhelms (1987) mapped other parts of SP-A's rings, shown as long dashed lines in Fig. 2A and B (labels T). In some cases the agreement with the best-fit and outer ellipse is good, particularly in the east. However, in the west and northwest there are several mapped locations that appear unrelated to either topographic ellipse (Fig. 2A). For our outer ellipse to extend westward and match the ring mapped by Wilhelms (1987) would require an almost perfectly circular outer ellipse and a westward shift of the basin center (Wilhelms used a center 11° west of our center). In that case, the outer ellipse would differ substantially from the centers and axial ratios of the best-fit topographic ellipse, the thorium ellipse, and the iron ellipse, and it would then no longer arc around the polar topography at P in Fig. 4. These considerations favor our outer ellipse for defining the western limit of the basin.

In summary, the validity of the outer ellipse is supported by (1) its derivation from a smaller best-fit topographic ellipse that is correlated with similarly elliptical geochemical data (Sections 3.3–4), (2) its passage through high topography around an arc of ~100° from the north to the east, and another arc near the south pole, and (3) its correlation with arcuate massifs at two locations on opposite sides of the basin. In all, the SP-A depression is about 2400 km long by 2050 km wide, approximately the same size as the main depression of the Hellas basin on Mars (~2300 km), and larger than the lunar radius by a factor of 1.4.

3.6. Regional trends in topography, chemistry, and mineralogy

A major trend in topography is that elevations are generally higher within the northern half of the best-fit topographic ellipse. This is most apparent when comparing the high elevations east of Mare Ingenii, west of Apollo, and south of label A in Fig. 1A, with low elevations south of the ellipse center. Another trend is that the topographic contours are generally sharper in the north than in the south. While the topographic contour around the outer ellipse in the northeast and east is almost unbroken, it is much less obvious or nonexistent in the west.

As shown in Fig. 2C and D, the topographic ellipses also border the main concentrations of thorium and iron in SP-A. Both iron and thorium are in higher abundances in the northern halves of the topography and elemental abundance ellipses. For thorium, the

outer topographic ellipse tightly borders the lowest thorium abundances in the north, while in the south the best-fit ellipse does the same, consistent with the thorium's more northern center. The Outer Terrace has little thorium in its southern half, but thorium is significantly more abundant in its northern portions. The northwest thorium anomaly also curves around the best-fit ellipse. For iron, the outer topographic ellipse also borders the lowest abundances of iron in the north and northeast. High abundances of iron (> wt. 8%) appear to extend over the best-fit topographic ellipse into the Outer Terrace in the north. Iron abundances are generally lower in the southern and southeastern parts of the Outer Terrace.

In Fig. 5A and B we plot the topographic ellipses over Clementine 750-nm reflectance data (A) and the band ratios from Pieters et al. (1994) (B). Fig. 5A shows that the best-fit topographic ellipse bounds the low-albedo mafic anomaly that is characteristic of the basin (Belton et al., 1992; Pieters et al., 1997). Fig. 4B shows that the interior of the basin is generally orange with lighter shades of green and yellow, suggesting higher abundances of iron-rich mineralogies. The feldspathic highlands terrain north of SP-A is generally red, purple, or blue, and represents more feldspar-rich units. The best-fit topographic ellipse tightly bounds the brightest regions of orange iron-rich material, while the outer ellipse separates much of the remaining orange iron-rich material from the blue-red highlands material. Similar to the gamma-ray derived iron observed in the northern Outer Terrace (Fig. 2D), iron-rich units are seen extending north of the best-fit topographic ellipse, in some cases reaching just beyond the outer ellipse. In all, the agreement between the best-fit topographic ellipse and the mafic mineralogy of the basin is quite strong.

4. Interpretation and discussion

4.1. Basin formation

On the basis of detailed analysis of the distributions of topography, iron and thorium, we suggest that an oblique impact caused the ellipse-shaped features and north–south asymmetries of excavation of lower crustal materials. The obliquity of the impact resulted in two major excavation structures that are represented by topography: the Outer Terrace, whose border approximately follows $\sqrt{2}$ ring scaling in semiminor axis, and a more deeply excavated central region that contains nearly all of the geochemical and mineralogical anomalies characteristic of the basin.

The first part of the hypothesis, that the basin was formed by an oblique impact, is well supported by data that show low-angle impacts cause elliptical craters (Melosh, 1989). Laboratory experiments indicate that at low energies elliptical structure appears only at low impact angles ($\sim$12° threshold from the horizontal for planetary surfaces (Bottke et al., 2000)). However, since the scale of the SP-A basin is so much larger than experimentally-produced elliptical craters and the diameter of the basin is larger than the planetary radius, it is uncertain if a constraint on the impactor angle with the surface normal can be inferred from existing experimental data.

Pike and Spudis (1987) argued that scaling of ring diameters by multiples of $\sqrt{2}$ is a statistically-valid feature of large circular impact basins on the Moon. A number of hypotheses have been advanced to explain the scaling of ring diameters in basins (Hodges and Wilhelms, 1978; McKinnon and Melosh, 1978; Pascal and Piette, 1999; Pike and Spudis, 1987; van Dorn, 1968), but no work has been done to address how rings scale in elliptical basins. However, three unique features of SP-A's ring structure are worth noting because they may provide some clues to its ring-forming mechanism, and the mechanism of ring formation in general. The first is that the scaling factor for SP-A's outer ellipse is different for the semiminor and semimajor axis (1.428 and 1.238, respectively, Table 1), which suggests a scaling rule that changes as a function of the azimuth from the basin center. The second is that there is strong correlation of the most clearly manifested outer ellipse sections with high topography in the northeast and east, suggesting that preexisting high topography may have a role in determining which areas develop rings. The third is that the Outer Terrace generally has a less mafic character than the interior of the basin (Section 3.6), and may therefore represent upper crustal materials which slumped inwards, as suggested by (Head, 1974). High-resolution multispectral data, terrain mapping images, and superior gravity measurements of the Outer Terrace may help resolve the exact mechanism for its formation.

4.2. Asymmetrical excavation and direction of impact

Several observations suggest that depth of excavation was asymmetrical along the direction of impact: (1) higher iron and

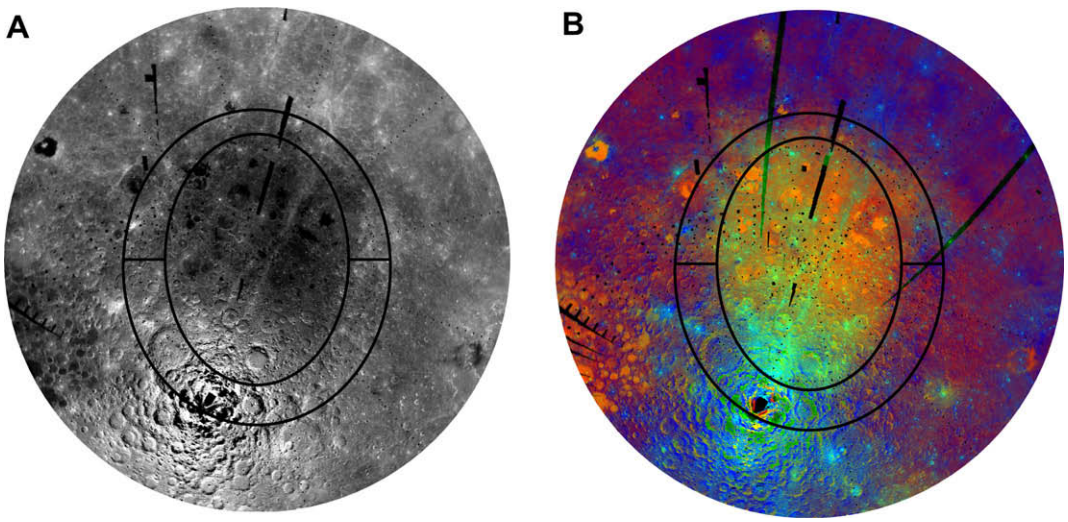

Fig. 5. Best-fit topographic ellipse and derived outer ellipses draped over: (A) Clementine 750-nm reflectance data, and (B) band ratio technique from Pieters et al. (1994). The projection is stereographic centered on the best-fit topographic ellipse center (−53.2°, 191.1°E) and rotated 18.8° clockwise. The limit of the projection is 60° of latitude and gridline spacing is 30°. Data near the poles suffer from high phase-angle artifacts, but are shown to aid in the identification of features.

thorium abundances in the north, (2) thorium and iron ellipses displaced north of the topographic ellipse, (3) a smaller and more circular thorium ellipse. In the Moon both iron and thorium are expected to increase in concentration with depth, and there is support for this in remote sensing observations (Lawrence et al., 1999; Metzger et al., 1977; Wieczorek and Phillips, 1997). The higher abundances of these elements in the northern halves of their ellipses suggest that depth of excavation became progressively deeper moving northwards. This is also supported by the more northern displacements of these ellipses compared to the topographic ellipse. Thorium is a surrogate for KREEP, which is generally believed to have crystallized in a layer between the mantle and lower crust. Thorium is expected to appear at a greater and more well-defined depth than iron due to its incompatibility and late crystallization. Therefore, if the depth of excavation increased northward, the thorium ellipse would be displaced to the north more than either the iron or topographic ellipses. The ellipse would also be smaller due to the smaller area of the most deeply exposed material. These predictions are what are observed in the actual thorium distribution (Fig. 2C).

It is possible that the putative north–south asymmetry in depth of excavation is a result of differences between the up-range and down-range excavation flow fields. Supporting this possibility are asymmetries such as sharper topography, thorium, and iron contours in the north, as well as higher topography. Mare volcanism is also much more prevalent in the north, with 90% of the total volume of basalts extruded located north of −55°, using the volumes and flow units identified by (Yingst and Head, 1997). Notably, the four largest craters in the northern half of SP-A, Ingenii (−33.7°, 163.5°E, 315 km), Apollo (−36.1°, 208.2°E, 537.0 km), Leibnitz (−38.3°, 179.2°E, 245.0 km) and Poincare (−56.7°, 163.6°E, 319.0 km, more central), are all nearly flooded with mare basalts, while the three largest and comparable size basins in the south, Planck (−57.9°, 136.8°E, 314.0 km), Schrödinger (−75.0°, 132.4°E, 312.0 km) and Zeeman (−75.2°S, 226.4°E, 190.0 km) are not at all, or are at least much less so (Shoemaker et al., 1994; Wilhelms et al., 1979). The greater abundance of volcanism in the north could be a reflection of regionally thinner crust or crust that is more mafic, either of which may have been an effect of asymmetry of excavation. The former would facilitate eruption via the overpressurized dyke model of (Head and Wilson, 1992), while the later would facilitate eruption via the buoyancy-controlled model of (Wieczorek et al., 2001).

An alternative explanation for the north–south asymmetries inside of SP-A is that the thorium was higher in the north prior to the impact, and the other asymmetries are secondary post-basin effects. In this case, the high abundance of mare basalts in the north could be related to the higher abundance of thorium and associated heat producing elements in the north, a correlation that is also observed in the nearside Procellarum KREEP Terrane (Jolliff et al., 2000). The higher surficial abundances of iron in the north, as well as in the plains of cryptomaria southwest of Apollo (Pieters et al., 2001), could then be largely due to increased mare abundances. Obviously, the exact cause and effect relationships between geochemistry, geology, and geophysics of the region, and how pre- or post-excavation processes affected them, are complex and interrelated. In fact, many of these issues in SP-A are at the heart of long-debated problems in global lunar evolution, such as the mechanism that controls mare basalt eruption (Elkins-Tanton et al., 2004; Head and Wilson, 1992; Wieczorek et al., 2001), the role of heat producing elements in controlling magma production (Parmentier et al., 2002), viscous relaxation of large basins (Solomon et al., 1982; Zhong and Zuber, 2000), and the depth of excavation of large basins (Pieters et al., 2001; Wieczorek and Phillips, 1999). Despite this complexity, however, the elliptical shape and north–south alignment of SP-A's mineralogical and geochemical signatures suggest that the basin forming event, as well as the impactor trajectory, played an important role in determining the gross structures and relationships we see now.

It will not likely be possible to use the basin's north–south asymmetries to confidently determine the direction of the impactor until future missions return superior farside gravity data, and better models of large oblique impacts are developed. Schultz has argued for an up-range displacement of the uplifted central peak in oblique impacts (Schultz, 1992a,b; Schultz and Anderson, 1996), but these findings are disputed (Ekholm and Melosh, 2001; McDonald et al., 2008; Shuvalov, 2003). Ekholm and Melosh (2001) appear to consent to a model where simple craters may be deeper up-range, but argue that in complex craters the modification stage may undo this effect. More recent simulations (Elbeshausen et al., 2007; Poelchau et al., 2007) and field work (Scherler et al., 2006) show evidence for asymmetries in central peak formation, but it is unclear if these asymmetries would be noticeable from orbital measurements. In all of these studies, the craters were much smaller, or much less elliptical than SP-A, making it uncertain how they would apply to SP-A.

4.3. Farside topography and lunar orientation

The highest lunar farside topography is almost exclusively on the eastern side of SP-A's long axis (Zuber et al., 1994), which suggests that it cannot be entirely due to emplaced SP-A ejecta. Ejecta from an oblique impact may have up-range/down range asymmetries, and a "forbidden zone" along the trajectory of impact (Melosh, 1989), but there is no existing model that would preferentially produce ejecta on one side of the axis along the impact direction. In fact, Jolliff et al. (2000) find evidence in the iron distribution around SP-A that its ejecta may be distributed on both sides of the trajectory axis, as often observed for smaller oblique impacts. Therefore, the high central farside topography most likely predates SP-A.

The lunar principal moments of inertia, and thereby the orientation of the Moon, are affected by basins as large as SP-A (Melosh, 1975), and the elliptical structure of SP-A defined here can help quantify its contribution. Even small angular changes in lunar orientation (∼10°) would be of interest, since a number of large-scale geologic and geophysical observations may be related to the history of the lunar orientation. For example, the lunar center of figure is displaced from its center of mass in the direction of the Earth–Moon axis within ∼24° (Smith et al., 1997), even though any arbitrary orientation is physically stable. The most stable position for a large uncompensated basin on a spherical Moon affected by tidal forces would be at the poles, and generally away from the sub-Earth and anti-Earth positions (0° and 180° longitudes) if there is preexisting J_2 gravitational potential. However, the basin is centered at (−53°, 191°E), suggesting that competing contributions to the global moments of inertia have affected its migration to the most stable location. It is possible that the changing compensation state of the basin with time has changed its contribution to the global moments of inertia and lunar orientation. Better farside gravity and an understanding of SP-A's state of compensation will help determine SP-A's contribution to the lunar orientation.

5. Conclusions

On the basis of the distributions of topography, thorium, and iron, we propose that the South Pole-Aitken basin is an elliptical structure with axes measuring 2400 by 2050 km and centered at (53°S, 191°E). Within the best-fit ellipses, iron, thorium, and high topography are preferentially found in the north, suggesting that an oblique impact effected the north–south alignment of their

distributions. A second, outer topographic ellipse is found to have a semiminor axis of $\sim\sqrt{2}$ times the best-fit topographic ellipse semiminor axis, which suggests a ring-scaling rule that is dependent on azimuth from the basin center. The outer ellipse is a discontinuous ring that is well defined near the south pole and in the northeast where surrounding topography is high, but is much weaker in the west. The best-fit topographic ellipse defines a much stronger geochemical anomaly and contains the main thorium and iron anomalies. Material between the outer ellipse and best-fit ellipse (the Outer Terrace) is of intermediate composition between the basin interior and surrounding highlands, suggesting that deeper materials were not excavated there. Because SP-A is a large, multiring and elliptical structure, which exhibits $\sim\sqrt{2}$ scaling in only one axis, it is a unique laboratory for understanding the generation and scaling of rings, elliptical crater formation, and the formation of massive basins in general (Andrews-Hanna et al., 2008; Marinova et al., 2008).

Acknowledgments

This work was supported by the NASA Planetary Geology and Geophysics Program. We are grateful to Jeff Andrews-Hanna for helpful discussions and Jody Russell (Johnson Space Center) for scans of Apollo 8 negatives.

References

Andrews-Hanna, J.C., Zuber, M.T., Banerdt, W.B., 2008. The Borealis basin and the origin of the martian crustal dichotomy. Nature 453, 1212–1215.
Archinal, B.A., Rosiek, M.R., Kirk, R.L., Redding, B.L., 2006. The unified lunar control network 2005. US Geological Survey Open-file Report 2006-1367.
Belton, M.J.S., and 10 colleagues, 1992. Lunar impact basins and crustal heterogeneity: New western limb and far side data from Galileo. Science 255, 570–576.
Bottke, W.F., Love, S.G., Tytell, D., Glotch, T., 2000. Interpreting the elliptical crater populations on Mars, Venus, and the Moon. Icarus 145, 108–121.
Ekholm, A.G., Melosh, H.J., 2001. Crater features diagnostic of oblique impacts: The size and position of the central peak. Geophys. Res. Lett. 28, 623–626.
Elbeshausen, D., Poelchau, M., Wünnemann, K., Kenkmann, T., 2007. Structural signatures of oblique impacts – Insights from numerical modeling. Workshop on Impact Cratering II, pp. 45–46.
Elkins-Tanton, L.T., Hager, B.H., Grove, T.L., 2004. Magmatic effects of the lunar late heavy bombardment. Earth Planet. Sci. Lett. 222, 17–27.
Garrick-Bethell, I., 2004. Ellipses of the South Pole-Aitken basin: Implications for basin formation. Proc. Lunar Sci. Conf. 35th, p. 1515.
Garrick-Bethell, I., Zuber, M.T., 2005. An indigenous origin for the South Pole-Aitken basin thorium anomaly. Geophys. Res. Lett. 32, L13203.
Hartmann, W.K., Kuiper, G.P., 1962. Concentric structures surrounding lunar basins. Commun. Lunar Planet. Lab. 1, 55–66.
Haskin, L.A., 1998. The Imbrium impact event and the thorium distribution at the lunar surface. J. Geophys Res. 103, 1679–1689.
Haskin, L.A., McKinnon, W.B., Benner, L.A.M., Joliff, B., 2004. Thorium anomalies in the NW quadrant of the South Pole-Aitken basin. Proc. Lunar Sci. Conf. 35th, p. 1461.
Head III, J.W., 1974. Orientale multi-ringed basin interior and implications for the petrogenesis of lunar highland samples. The Moon 11, 327–356.
Head III, J.W., Wilson, L., 1992. Lunar mare volcanism: Stratigraphy, eruption conditions, and the evolution of secondary crusts. Geochim. Cosmochim. Acta 56, 2155–2175.
Hiesinger, H., Head III, J.W., 2004. Lunar South Pole-Aitken basin: Topography and mineralogy. Proc. Lunar Sci. Conf. 35th, p. 1164.
Hodges, C.A., Wilhelms, D.E., 1978. Formation of lunar basin rings. Icarus 34, 294–323.
Jolliff, B.L., Gillis, J.J., Haskin, L.A., Korotev, R.L., Wieczorek, M.A., 2000. Major lunar crustal terranes: Surface expressions and crust-mantle origins. J. Geophys. Res. 105, 4197–4216.
Lawrence, D.J., Feldman, W.C., Barraclough, B.L., Binder, A.B., Elphic, R.C., Maurice, S., Miller, M.C., Prettyman, T.H., 2000. Thorium abundances on the lunar surface. J. Geophys. Res. 105, 20307–20332.
Lawrence, D.J., Feldman, W.C., Elphic, R.C., Little, R.C., Prettyman, T.H., Maurice, S., Lucey, P.G., Binder, A.B., 2002. Iron abundances on the lunar surface as measured by the Lunar Prospector gamma-ray and neutron spectrometers. J. Geophys. Res. 107, 5130.
Lawrence, D.J., Elphic, R.C., Feldman, W.C., Prettyman, T.H., Gasnault, O., Maurice, S., 2003. Small-area thorium features on the lunar surface J. Geophys. Res. 108, 5102.
Margot, J.L., Campbell, D.B., Jurgens, R.F., Slade, M.A., 1999. Topography of the lunar poles from radar interferometry: A survey of cold trap locations. Science 284, 1658–1670.
Marinova, M.M., Aharonson, O., Asphaug, E., 2008. Mega-impact formation of the Mars hemispheric dichotomy. Nature 453, 1216–1219.
McDonald, M.A., Melosh, H.J., Gulick, S.P.S., 2008. Oblique impacts and peak ring position: Venus and Chicxulub. Geophys. Res. Lett. 35, L07203.
McKinnon, W., Melosh, H.J., 1978. The mechanism of ringed basin formation. Geophys. Res. Lett. 5, 985–988.
Melosh, H.J., 1975. Large impact craters and the Moon's orientation. Earth Planet. Sci. Lett. 26, 353–360.
Melosh, H.J., 1989. Impact Cratering: A Geologic Process. Oxford University Press.
Metzger, A.E., Haines, E.L., Parker, R.E., Radocinski, R.G., 1977. Thorium concentrations in the lunar surface. I: Regional values and crustal content. Proc. Lunar Sci. Conf. 8th, pp. 949–999.
Parmentier, E.M., Zhong, S., Zuber, M.T., 2002. Gravitational differentiation due to initial chemical stratification: Origin of lunar asymmetry by the creep of dense KREEP? Earth Planet. Sci. Lett. 201, 473–480.
Pascal, A., Piette, T., 1999. Small-scale models of multiring basins. J. Geophys. Res. 104, 16501–16514.
Petro, N.E., Pieters, C.M., 2004. Surviving the heavy bombardment: Ancient material at the surface of South Pole-Aitken Basin. J. Geophys. Res. 109, E06004.
Pieters, C.M., Staid, M.I., Fischer, E.M., Tompkins, S., He, G., 1994. A sharper view of impact craters from Clementine data. Science 266, 1844–1848.
Pieters, C.M., Tompkins, S., Head III, J.W., Hess, P.C., 1997. Mineralogy of the mafic anomaly in the South Pole-Aitken Basin: Implications for excavation of the lunar mantle. Geophys. Res. Lett. 24, 1903–1906.
Pieters, C.M., Gaddis, L., Jolliff, B., Duke, M., 2001. Rock types of South Pole-Aitken basin and extent of basaltic volcanism. J. Geophys. Res., 28001–28022.
Pike, R.J., Spudis, P.D., 1987. Basin-ring spacing on the Moon, Mercury, and Mars. Earth, Moon Planets 39, 129–194.
Poelchau, M., Elbeshausen, D., Kenkmann, T., Wünnemann, K., 2007. Structural signatures of oblique impacts – Insights from field observations. Workshop on Impact Cratering II, pp. 99–100.
Rosiek, M.R., Aeschliman, R., 2001. Lunar shaded relief map updated with Clementine data. Proc. Lunar Sci. Conf. 32nd, p. 1943.
Scherler, D., Kenkmann, T., Jahn, A., 2006. Structural record of an oblique impact. Earth Planet. Sci. Lett. 248, 43–53.
Schultz, P.H., 1992a. Atmospheric effects on ejecta emplacement and crater formation on Venus from Magellan. J. Geophys. Res. 97 (16), 16,183–16,248.
Schultz, P.H., 1992b. Effect of impact angle on central peak/peak ring formation and crater collapse on Venus. LPI-Papers Presented to the International Colloquium on Venus, pp. 103–104.
Schultz, P.H., 1997. Forming the South-Pole Aitken basin: The extreme games. Proc. Lunar Sci. Conf. 28th, p. 1787.
Schultz, P.H., Anderson, R.R., 1996. Asymmetry of the Manson impact structure: Evidence for impact angle and direction. Geol. Soc. Am., 397–417.
Shevchenko, V.V., Chikmachev, V.I., Pugacheva, S.G., 2007. Structure of the South Pole-Aitken Lunar Basin. Solar Syst. Res. 41, 447–462.
Shoemaker, E.M., Robinson, M.S., Eliason, E.M., 1994. The south pole region of the Moon as seen by Clementine. Science 266, 1851–1854.
Shuvalov, V.V., 2003. Cratering process after oblique impacts. In: Third International Conference on Large Meteorite Impacts, p. 4130.
Smith, D.E., Zuber, M.T., Neumann, G.A., Lemoine, F.G., 1997. Topography of the Moon from the Clementine lidar. J. Geophys. Res. 102, 1591–1611.
Solomon, S.C., Comer, R.P., Head, J.W., 1982. The evolution of impact basins: Viscous relaxation of topographic relief. J. Geophys Res. 87, 3975–3992.
Spudis, P.D., 1993. Geology of Multiring Basins. Cambridge University Press, Cambridge.
Spudis, P.D., Reisse, R.A., Gillis, J.J., 1994. Ancient multiring basins on the Moon revealed by Clementine laser altimetry. Science 266, 1848–1851.
Spudis, P.D., Plescia, J., Bussey, B., Josset, J.-L., Beauvivre, S., 2008. The geology of the south pole of the Moon and age of Shackleton crater. Proc. Lunar Sci. Conf. 39th, p. 1626 (abstract).
Stuart-Alexander, D.E., 1978. Geologic map of the central far side of the Moon. US Geol. Surv. Map, I-1047.
van Dorn, W.G., 1968. Tsunamis on the Moon? Nature 220, 1102–1107.
Wieczorek, M.A., Phillips, R.J., 1997. The structure and compensation of the lunar highland crust. J. Geophys Res. 102, 10933–10943.
Wieczorek, M.A., Phillips, R.J., 1999. Lunar multiring basins and the cratering process. Icarus 139, 246–259.
Wieczorek, M.A., Zuber, M.T., 2001. A Serenitatis origin for the Imbrian grooves and South Pole-Aitken thorium anomaly. J. Geophys Res. 106, 27853–27864.
Wieczorek, M.A., Zuber, M.T., Phillips, R.J., 2001. The role of magma buoyancy on the eruption of lunar basalts. Earth Planet. Sci. Lett. 185, 71–83.
Wilhelms, D.E., 1987. The geologic history of the Moon. US Geological Survey.
Wilhelms, D.E., Howard, K.A., Wilshire, H.G., 1979. Geologic map of the south side of the Moon. USGS special report I-1162, US Geological Survey, Reston, VA.
Wood, C.A., Gifford, A.W., 1980. Evidence for the lunar big backside basin. Conference on Multi-ring Basins: Formation and Evolution, p. 414.
Yingst, A.R., Head III, J.W., 1997. Volumes of lunar lava ponds in South Pole-Aitken and Orientale basins: Implications for eruption conditions, transport mechanisms, and magma source regions. J. Geophys. Res. 102, 10,909–10,931.
Zhong, S., Zuber, M.T., 2000. Long-wavelength topographic relaxation for self-gravitating planets and implications for the time-dependent compensation of surface topography. J. Geophys. Res. 105, 4153–4164.
Zuber, M.T., Smith, D.E., Lemoine, F.G., Neumann, G.A., 1994. The shape and internal structure of the Moon from the Clementine mission. Science 266, 1839–1843.